Asian Journal of Chemistry; Vol. 36, No. 7 (2024), 1559-1570

ASIAN JOURNAL OF CHEMISTRY

https://doi.org/10.14233/ajchem.2024.31377

A Green Approach: *Syzygium aromaticum* Mediated Synthesis of CuO Nanoparticles with Potential for Wastewater Treatment

PARNEET KAUR[1], SANJEEV KUMAR[1,*], HARPREET KAUR[1,*], SANJEEV KUMAR[1], JYOTI GAUR[2] and DIKSHA RANI[1]

[1]Department of Physics, Chandigarh University, Gharuan, Mohali-140413, India
[2]School of Basic and Applied Sciences, RIMT University, Mandi Gobindgarh-147301, India

*Corresponding authors: E-mail: kumarsanju25@gmail.com; mann.khant91@gmail.com

Received: 10 February 2024; *Accepted*: 8 May 2024; *Published online*: 29 June 2024; AJC-21675

The growing demand for environmentally sustainable and economically viable techniques for synthesizing nanoparticles is driving the advancement of green nanotechnology. This study presents an innovative approach for synthesizing copper oxide nanoparticles (CuO NPs) by utilizing an extract derived from *Syzygium aromaticum*. The XRD analysis verified the reliable synthesis of CuO, as indicated by the presence of the monoclinic phase and the extremely small crystallite size of 7.89 nm. FTIR spectrum illustrated the functionalizing of CuO with *S. aromaticum* phytochemicals, whereas FE-SEM and HR-TEM micrographs demonstrate the intricate nanostructure of the NPs. The SAED signals provide further confirmation of the crystalline structure. The clear existence of a well-defined absorption peak at 276 nm and an energy band gap of 3.58 eV undeniably confirms the effective synthesis of CuO NPs. Furthermore, the synthesized nanoparticles showed exceptional capability in degrading the resilient pollutant Congo red dye. By applying a dosage of 200 mg L^{-1}, a remarkable 97% removal of Congo red dye (100 mg L^{-1}) was achieved after 100 min following the pseudo-first-order kinetics.

Keywords: Green nanotechnology, Biogenic CuO nanoparticles, Congo red dye, *Syzygium aromaticum*, Photocatalysis.

INTRODUCTION

The global water crisis presents a formidable and imminent threat to humanity, exacerbated by the relentless contamination of our water bodies with industrial wastewater [1]. Among the major culprits in this environmental degradation is the textile industry, responsible for the prodigious annual discharge of 80×10^4 tons of azo dyes, the synthetic colourants that lend vibrancy to textiles [1,2]. Synthesized using hazardous aromatic hydrocarbons like benzene, toluene, naphthalene, phenol and aniline, these dyes contribute significantly to water pollution as 10-15% remain unfixed to textile materials during production, leading to resource loss and environmental damage [3]. Upon entering aquatic ecosystems, azo dyes pose severe ecological threats by increasing the chemical and biological oxygen demand, disrupting pH levels and altering the inorganic composition of water bodies. This necessitates the urgent development of effective mitigation strategies to combat the impact of industrial activities, particularly in the textile industry, on our precious water resources.

Nanotechnology is increasingly recognized as a transformative solution in the field of wastewater treatment, namely in addressing the long-standing issue of azo dye pollution. Nanocatalysis plays a significant role in advanced oxidation processes (AOPs) and has great promise. Significantly, advanced oxidation processes (AOPs) such as sonochemical oxidation, electrochemical oxidation and the photo-Fenton reaction produce potent oxidizing agents (such as hydroxyl radicals) that efficiently break down intricate dye molecules into less complicated and less harmful substances [4]. Furthermore, the process concludes with the safe discharge of carbon dioxide and water, reducing the environmental impact in contrast to the traditional methods.

Copper oxide nanoparticles (CuO NPs) dominate the field of photocatalysis due to their exceptional properties and metrics that validate their status as exemplary photocatalysts. The electrical structure of CuO is optimized because of its low bandgap, which has been accurately determined to be in the range of 1.2 to 4 eV [5]. This attribute encompasses the ability to effectively absorb light across the UV, visible and near-infrared

spectra, hence optimizing the utilization of solar energy. Therefore, CuO is notable for its high efficiency as a photocatalyst due to its exceptional ability to capture light. The redox potentials of CuO, namely the +0.15 V (*vs.* NHE) for the Cu^{2+}/Cu^{+} redox couple, explain its successful catalytic performance [6]. The numerical affirmation emphasizes the ability of CuO to easily separate charge carriers and undergo redox transformations, which are essential for many photocatalytic reactions. The electron affinity of CuO, which is measured to be roughly 0.15 eV, enhances charge carrier dynamics, reducing recombination and assuring a high quantum efficiency in photocatalytic processes [7]. CuO has a large surface area of around 35 m^2/g, which allows for a wide range of catalytic processes [8]. The numerical value leads to an increased number of active sites, enhancing its ability to catalyse reactions and making CuO a highly attractive option for many photocatalytic applications. The recorded breakdown temperature of CuO, which is around 600 ºC, highlights its thermal stability [9]. This value represents the ability of CuO to withstand photocatalytic conditions, allowing for long-lasting and efficient exploitation without affecting its catalytic efficiency. When exposed to light, CuO demonstrates its ability by revealing a hydroxyl radical generation rate of around 0.2 $\mu mol/g^{-1}$ h^{-1} [10]. This quantification not only demonstrates the inherent reactivity of CuO but also expands its potential applications in environmental remediation, highlighting its versatility and significant influence as a photocatalyst.

The use of plant extracts for synthesizing diverse nanomaterials has gained significant traction in recent years, offering several advantages. Firstly, these methods are cost-effective, as plant extracts are readily available and often less expensive than conventional chemicals used in nanoparticles synthesis. Additionally, plant-based approaches are biocompatible, showing lower toxicity and better compatibility with biological systems compared to synthetic materials. Several studies highlight the successful synthesis of CuO nanoparticles using various plant extracts. Examples include *Punica granatum* leaves, *Penicillium fungi* and specific leaf extracts such as *Ocimum sanctum*, *Abies spectabilis, Stachys lavandulifolia*, *Catha edulis* and *Parthenium hysterophorus* [11-16]. *Syzygium aromaticum*, derived from the dried flower buds of an Indonesian tree, contains active ingredients such as eugenol and acetyl eugenol [17]. Eugenol, responsible for *Syzygium aromaticum's* aroma, possesses antimicrobial and antioxidant properties, making it an attractive choice for nanoparticle development. The rich phytochemical profile of *S. aromaticum* underscores its potential for eco-friendly and biocompatible nanoparticles synthesis.

Numerous studies have shown the versatile applications of CuO NPs synthesized through plant extracts. In a study conducted by Vidovix *et al.* [18], CuO NPs synthesized with *Punica granatum* leaf extract exhibited an outstanding 96.91% removal efficiency of methylene blue dye, highlighting their potential for wastewater treatment. Usha *et al.* [19] reported a green synthesis of CuO NPs using *Streptomyces* sp., demonstrating their application in developing antimicrobial textiles to counter hospital-acquired infections. Moreover, Ganesan *et al.* [20] harnessed *Acalypha indica* leaf extract to synthesize CuO NPs with promising dual capabilities in cancer therapy and dye degradation. These nanocomposites displayed 70% cytotoxic activity against human colon cancer cells and an 83.20% efficiency in degrading methylene blue dye, highlighting their potential in biomedical and environmental contexts. Similarly, Kaur *et al.* [21] facilitated the synthesis of CuO NPs with *Punica granatum* extract with enhanced photocatalysis efficiencies up to 97.8%, emphasizing their effectiveness in the dye decolourization.

The resistance of azo dyes to biodegradation and their resulting environmental impact highlights the need for efficient mineralization in wastewater treatment systems. This research aims to utilize the enhance photocatalysis characteristics of green synthesized CuO NPs from *S. aromaticum* extract against the commonly used azo dye *i.e.* Congo red. This unique method entails a thorough analysis of the generated biomediated CuO NPs, with a specific focus on their structural, morphological and optical properties.

EXPERIMENTAL

All chemicals and solvents used in this work were obtained from Sigma-Aldrich, USA. The specific chemicals *i.e.* copper(II) acetate hydrate [$Cu(CO_2CH_3)_2{\cdot}2H_2O$, ≤ 99%], ammonia (≤ 30%) and ethanol (≤ 99.9%) were of highest purity. The synthesis of CuO NPs involved the utilization of bud extract derived from *Syzygium aromaticum*, sourced from the Punjab region in India (30.6355ºN, 76.3870ºE). To maintain the precision and reliability throughout the experimental work, double-distilled (DD) water and Whatman filter papers with a pore size of approximately 1.21 µm were employed.

***Syzygium aromaticum* bud extract:** *S. aromaticum* buds, commonly referred to as cloves, present a valuable repository of bioactive compounds with diverse potential medicinal properties [22]. This study introduces a refined extraction approach, emphasizing efficiency, environmental sustainability and the preservation of bioactive integrity. The initial phase involved a thorough cleansing of *S. aromaticum* buds with distilled water to eliminate any extraneous impurities. Subsequently, the purified buds underwent an air-drying process at room temperature. In order to optimize the extraction process, the dehydrated buds were subjected to a thorough grinding using a mill, therefore enhancing the available surface area for extraction. Afterwards, the powder obtained was allowed to soak in 80% ethanol for one day. Ethanol, selected for its efficiency in extracting a diverse range of phytochemicals from the buds, facilitated a comprehensive extraction process. The ethanol-based extract underwent careful vacuum filtration to eliminate insoluble particles. Following this, a further clarification step was executed through centrifugation at 10,000 rpm for 14 min, ensuring the removal of finer particles and enhancing the purity of the extract. The concentration of the alcoholic extract was achieved using a rotary evaporator to eliminate excess ethanol and the concentrated solution was then stored at room temperature to ensure the stability and preserve the inherent bioactive constituents. The utilization of a low-temperature procedure effectively reduces the risk of thermal degradation, hence preserving the structural integrity of volatile bioactive chemicals obtained from cloves.

Synthesis of CuO NPs using *Syzygium aromaticum* bud extract: The synthesis process was initiated by dissolving copper(II) acetate hydrate in distilled water at a controlled temperature of 70 ºC for an optimized duration of 25 min, ensuring complete solubilization of the precursor and the availability of copper ions for subsequent nanoparticle formation and then *S. aromaticum* bud extract was introduced. The naturally occurring phytochemicals act as potent reducing and stabilizing agents, facilitating the reduction of Cu^{2+} ions to CuO NPs while preventing agglomeration for uniform dispersion. The pH of the reaction medium was adjusted to 10 using NaOH, a critical step for controlling the morphology and size of the CuO NPs. By adjusting the pH, the conditions were optimized for the nucleation and development of nanoparticles, which leads to the precipitation of copper ions and the creation of CuO nuclei. Additionally, it enhances the deprotonation of phytochemicals extracted from *S. aromaticum*.

The synthesis procedure was further optimized by adjusting reaction time and temperature. The reaction mixture undergoes the reaction period of 45 min at the optimized temperature of 70 ºC, allowing the sufficient time for CuO nanoparticles growth and maturation. Following the carefully optimized synthesis steps, the precipitates were collected *via* filtration, subjected to thorough washing with distilled water and ethanol to remove impurities and dried at 80 ºC for 6 h. The obtained dried material was precisely pulverized to obtain CuO nanopowder of superior quality.

Characterization: To investigate the structural and compositional aspects of CuO NPs synthesized with *S. aromaticum* bud extract, an X-ray diffraction (XRD) pattern was recorded using a PANalytical XRD diffractometer. For the determination of band gap energy, a UV-visible spectrum was acquired using a Shimadzu UV–visible spectrophotometer, providing insights into the electronic structure and optical properties of the CuO NPs. Fourier transform infrared (FTIR) spectra of both the *S. aromaticum* bud extract and the CuO NPs were recorded using a Bruker FTIR spectrometer, facilitating the identification of functional groups and molecular interactions involved in the synthesis process. A high-resolution transmission electron microscope (HRTEM) from JEOL model JSM-6390 LV was utilized to observe the particle size and morphology at high magnification. Additionally, the scanning electron microscope (SEM) from Carl-Zeiss provided further insights into the surface morphology of the green synthesized CuO NPs. The elemental composition of the CuO NPs was determined using an energy dispersive X-ray detector (EDX) from model Oxford XMXN, facilitating the comprehensive analysis of elemental constituents.

Photocatalytic activity: In this study, the photocatalytic activity of green synthesized CuO NPs, exploring their effectiveness in degrading a common textile dye Congo dye was investigated. Understanding the many complexities of photocatalysis is our primary goal in this study, particularly discerning the effectiveness of *S. aromaticum* mediated CuO NPs in the degradation of Congo red dye, a ubiquitous textile dye, under UV irradiation. The experimental protocol unfolded systematically, encompassing the dispersion of different quantities of green synthesized CuO NPs (100 and 200 mg L^{-1}) within an aqueous Congo red solution. Following an equilibrium period for adsorption/desorption, the suspension underwent exposure to UV light under continuous agitation. At the fixed intervals of 20 min, 7 mL of samples were pipetted out. After separating nanoparticles and quantifying the residual dye concentration with a UV-Vis spectrometer, Congo red removal percentage was calculated using eqn. 1:

$$\text{Removal of Congo red dye } (\%) = \frac{C_o - C_t}{C_t} \times 100 \quad (1)$$

where C_o = the initial concentration in the absence of UV light and C_t = the final concentration of the Congo red dye solution at regular 20 min intervals during UV light exposure.

RESULTS AND DISCUSSION

XRD studies: The crystallinity, purity and size of the *S. aromaticum* mediated CuO NPs were identified with the X-ray diffraction (XRD) patterns at 2θ 33.29º, 36.22º, 39.45º, 49.49º, 54.22º, 58.90º, 62.28º, 66.99º, 68.50º, 73.07º, 75.64º, which were allocated to the planes (110), (002), (200), ($\bar{1}$12), ($\bar{2}$02), (020), (202), ($\bar{1}$13), (022), (220) as depicted in Fig. 1. The observed diffraction peaks were matched with the monoclinic CuO phase specified by JCPDS card no. 01-089-2531. The diffractograms showed no characteristic peak caused by any impurity, indicating the synthesis of the pure crystalline CuO phase. The XRD pattern obtained from the CuO NPs has well-defined peaks with significant broadening, suggesting a high level of crystallinity and a small crystallite size. The Debye-Scherrer's equation was used to determine the average size of the CuO NPs;

$$D = \frac{K\lambda}{\beta \cos\theta} \quad (2)$$

where λ is the wavelength of X-ray radiation, β is the full-width half maxima (FWHM) of the peaks at diffraction angle θ and K is a constant equal to 0.94. The FWHM for all indicated peaks was examined and calculated *via* Lorentz fitting of the curve, resulting in an R^2 value over 0.99. Upon calculating the crystallite sizes of all the peaks, the resulting value for the average crystallite size (D) was found to be 43.44 nm for CuO NPs synthesized from *S. aromaticum* bud extract.

Bragg's law was used to calculate the *d*-spacing and lattice constant parameters:

$$2d \sin\theta = n\lambda \quad (3)$$

where d is the inter-atomic spacing between planes, λ is the wavelength of the X-ray, n is the order of diffraction and θ diffraction angle. The cell volume was found to be 70.73 nm, while the dimensions of the unit cell have been determined as a = 4.58 nm, b = 3.12 nm and c = 4.95 nm. The volume of the monoclinic CuO unit cell, as determined for the synthesized sample, is 70.73 nm, far below the optimal value of 82.64 nm for the monoclinic structure (Table-1). There is a variation from the ideal volume that occurs as a result of grain reduction and compression, which may be attributed to the influence of lattice solidity.

UV-visible studies: The spectral peak resonance (SPR) absorption band of *S. aromaticum* bud extract mediated CuO

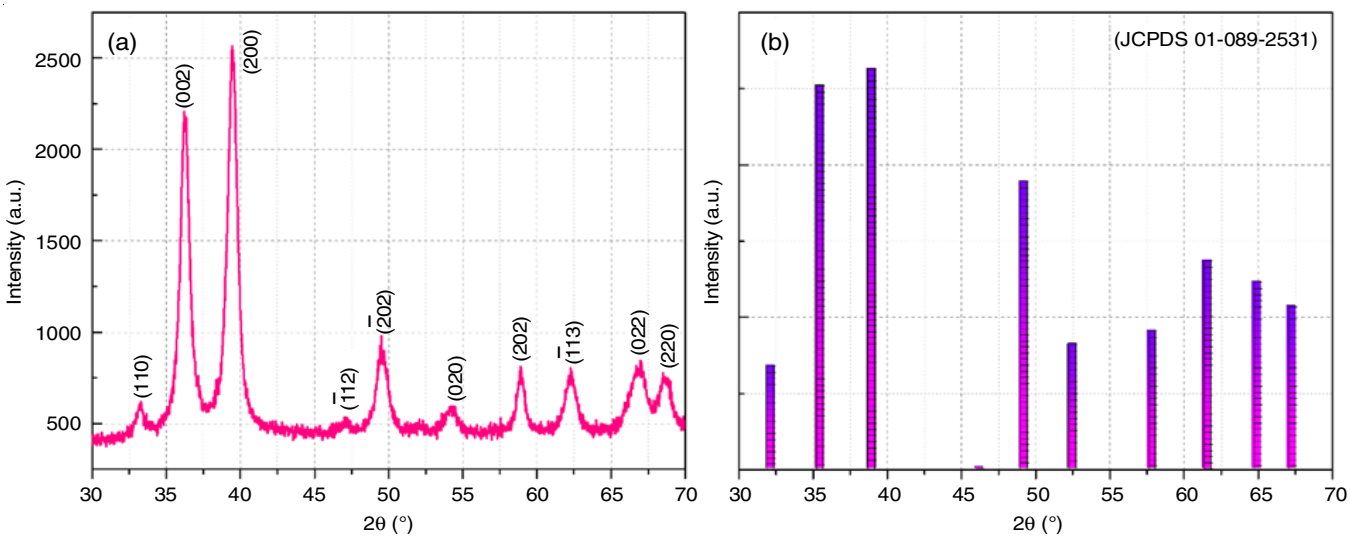

Fig. 1. X-ray analysis (a) XRD patterns of *S. aromaticum* mediated CuO NPs and (b) standard JCPDS

TABLE-1
STRUCTURAL AND GEOMETRICAL PARAMETERS OF *S. aromaticum* MEDIATED CuO NPs

2θ (°)	θ (radians)	θ (°)	β (radians)	d-spacing	D (nm)
33.2984	0.291	1.616	0.0282	2.68855	5.36
36.2224	0.316	0.775	0.0135	2.47795	11.27
39.4524	0.344	0.826	0.0144	2.28220	10.68
49.4994	0.432	1.042	0.0182	1.83994	8.77
54.2254	0.473	1.922	0.0335	1.69021	4.85
58.9004	0.514	0.790	0.0138	1.56671	12.06
62.2834	0.544	1.209	0.0211	1.48949	8.02
66.9924	0.585	1.710	0.0299	1.39577	5.82
68.5054	0.598	1.462	0.0255	1.36859	6.87
73.0784	0.638	1.571	0.0274	1.29381	6.57
75.6454	0.660	1.608	0.0281	1.25616	6.53
				Average crystallite size = 7.89 nm	

Lattice parameters	Calculated values	Experimental values
a (Å)	4.58	4.66
b (Å)	3.12	3.48
c (Å)	4.95	5.11
Cell volume (Å^3)	70.73	82.24

NPs emerged as a crucial indicator, prominently at 276 nm (Fig. 2a). The biosynthesized CuO NPs exhibited strong absorbance across the visible wavelength range (200-350 nm), emphasizing their potential for various applications [23]. Remarkably, a gradual decrease in the absorbance intensity with wavelength suggests the controlled and efficient formation of CuO NPs within a specific range. Tauc's plot was employed to analyze the band gap values of the CuO NPs. The extrapolation of the $(\alpha h\nu)^2$ *versus* (hν) plot unveiled a bandgap energy of 3.58 eV for the synthesized CuO NPs (Fig. 2b). The increased band gap indicates distinctive electrical characteristics, which may be impacted by the bioactive constituents present in the *S. aromaticum* extract.

FTIR studies: The green synthesized CuO NPs were examined in order to identify the potential biomolecules that may have contributed to the effective stabilization of the CuO NPs. The FTIR spectrum of *S. aromaticum* extract is illustrated in Fig. 3a. The extract exhibits distinct absorption bands at certain wavenumbers, which are suggestive of distinct molecular functionalities. Remarkably, the absorption peak at 3806 cm^{-1} is

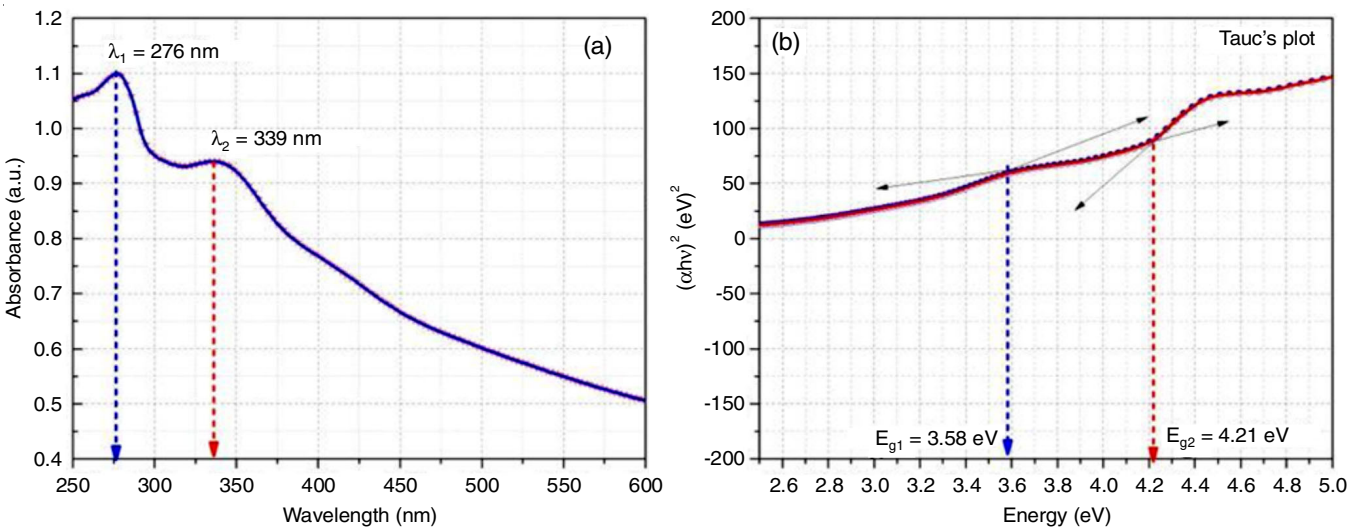

Fig. 2. (a) UV-vis pattern of *S. aromaticum* mediated CuO NPs and (b) Tauc's plot of CuO NPs

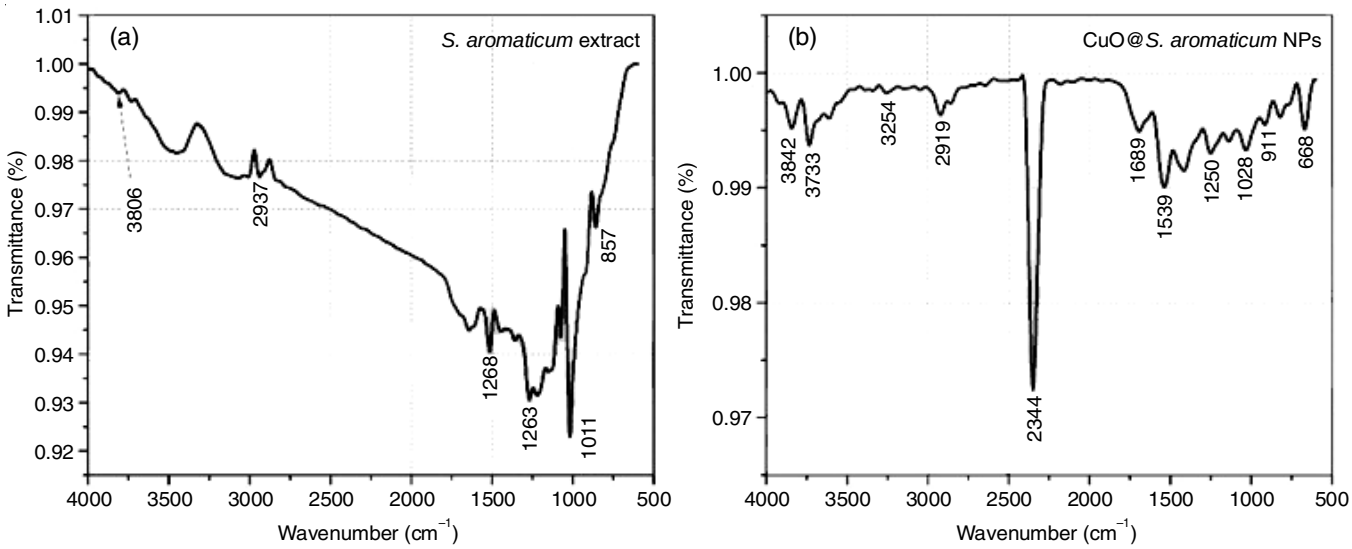

Fig. 3. FTIR spectra (a) *S. aromaticum* extract and (b) *S. aromaticum* mediated CuO NPs

ascribed to the stretching vibration of the alcoholic –OH group in eugenol and the –NH group prevalent in other phytochemicals. Furthermore, the presence of secondary amines appeared at 2937 cm^{-1}, corresponding to the asymmetric stretching of C–H and C–N groups. The C-O stretching band and the C-H bending vibration of the alkanes band are noticeable at 1268 cm^{-1} and 1263 cm^{-1}, respectively, enriching the spectrum with additional molecular insights. The amide-I vibrations at 1011 cm^{-1}, along with the aromatic stretching vibrations of –C=C– and carboxyl (C=O) stretching vibrations associated with protein amide bonds, contribute to the complexity of the spectrum. Moreover, the complex interaction of various compounds in the extract is evidenced by the emergence of a prominent peak at 857 cm^{-1}, indicative of multiple modes of vibration. The main compounds present in the extract of *S. aromaticum* are esters, phenyl propanoid, oxygenated sesquiterpenes and sesquiterpenes. Various compositions were reported in the ingredients including α-humulene (2.75%), caryophyllene (14.84%), eugenol (55.60%) and eugenyl acetate (20.54%). Additionally, there were trace amounts of β-elemene (0.04%), α-cadinene (0.05%) and ledol (0.06%). These findings are good matched with the GC-MS spectra of oil obtained from *S. aromaticum* [24].

In the FTIR spectrum of synthesized CuO NPs from the extract of *S. aromaticum*, several significant peaks emerged, for example, at 3842, 3733 and 3254 cm^{-1} signify the O-H bending vibrations, while the strong peaks at 2344 cm^{-1} and others at 1689 and 911 cm^{-1} revealed the C-H bending vibrations (Fig. 3b). The peaks at 1539 and 1028 cm^{-1} correspond to the stretching vibrations of the N-O group of nitro compounds and the C-O bond of phenols, respectively. Additionally, the aromatic stretching frequencies of C=O and C=C, as well as saturated hydrocarbons, are distinguished through peaks at 1250 cm^{-1}. A sharp absorption band at 668 cm^{-1} within the characteristic region of the CuO spectrum (4000–500 cm^{-1}) serves as a key indicator of the metal–oxygen or Cu-O stretching mode, thereby confirming the formation of CuO (Fig. 3b).

Morphological studies: The surface structure of the *S. aromaticum* bud extract mediated CuO NPs was examined using field-emission scanning electron microscopy (FESEM). The close inspection at 50 KX magnification (Fig. 4a) reveals a miniature of CuO NPs with a clear scale bar denoting a 200 nm length. The CuO NPs appear in this high-resolution image as interesting sphere clusters elongated in length and dispersed over a large area. The unique morphology is highlighted by the uniform spherical rod shape of both single and clustered nanoparticles. Moreover, the results indicated that the CuO NPs have a higher surface area due to their spherical elongated rod like topography [25]. The unique topography is a direct result of the significant effect of the plant extract, which influenced the arrangement of these linked spherical rod structures. Furthermore, Fig. 4b shows the results of increasing the FESEM magnification to an 100 KX times. Under this higher magnification, the examination of CuO NPs is intensified, verifying the existence of clusters with a characteristic cylindrical elongated shape consisting of a spherical clustered shape. These elongated cylindrical rods have an average diameter of less than 20 nm. Additionally, a closer look at individual spherical nanoparticles inside the rod shows an undetected size variety that falls within the 10 nm range and adds to the variability in the nanoparticles composition. The nanoparticles observed aggregations suggest a possible mechanism involving the existence of ionic bridges linking various phytochemical groups. This minor interaction helps CuO NPs to form stable clusters and clarifies the function of plant extract in supporting both the spherical form and complex interconnectivity of these nanostructures.

To investigate the elemental composition of the synthesized CuO NPs, X-ray spectroscopy in the form of energy-dispersive X-ray (EDX) analysis was also performed. The acquired spectra exhibited distinct peaks that corresponded to the components which were expected to be present in CuO (Fig. 4c). According to the study, the main elements are copper and oxygen, with atomic percentages of 58.44% and 41.56%, respectively and weight percentages of 84.81% and 15.19%. These results certainly underline the significant amount of copper and oxygen in the composition, closely agreeing with the ideal stoichiometry of CuO. These distinct peaks and the absence of any impurity peaks

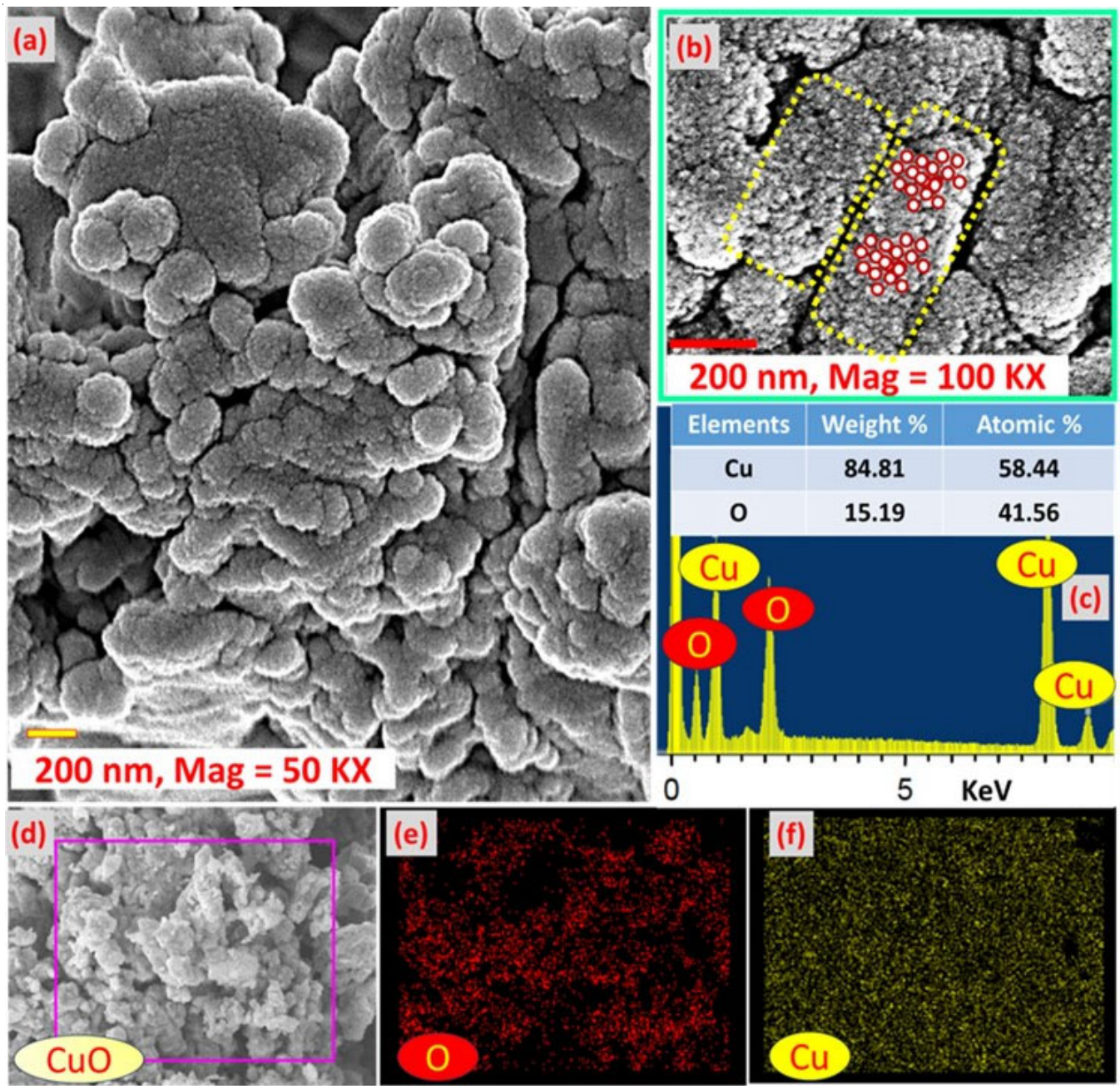

Fig. 4. *S. aromaticum* mediated CuO NPs through FESEM images (a) at 50,000x and (b) 100,000x magnifications. The corresponding EDX analyses include (c) the spectrum, (d) dot-mapped focus, (e) oxygen-mapped and (f) copper-mapped distributions

within the EDX detection range clearly support the purity of the synthesized CuO NPs.

Furthermore, the FESEM analysis revealed a uniform spherical topography with different levels of aggregation in every area of the sample as shown in Fig. 4d. A closer look at the distinct ways that the copper and oxygen atoms within the spherical forms aggregate shows an exceptional degree of homogeneity and spatial ordering of the atoms (NPs). In other words, the observed clusters indicate that the elements within the nanoparticles spread uniformly. As shown in Fig. 4d, there are clusters of moderately agglomerated and aggregated spherical particles. In spite of that a remarkable degree of dispersity has been maintained throughout the process.

Figs. 4e and 4f provide important information about the spatial distribution of copper and oxygen atoms in the green synthesized CuO sample. These maps provide a visual depiction of the concentration and arrangement of these components throughout the sample, with each dot representing the X-ray signal detected from a particular place. The oxygen atoms in the CuO sample are distributed uniformly and consistently as can be seen by analyzing the map in Fig. 4e. A uniform presence of oxygen within the material is suggested by the dots generally constant intensity in most places. The expected stoichiometry of CuO, which states that for each unit cell, an oxide ion (O^{2-}) bonds with copper ions, is consistent with this result. In the same manner, the copper dot map (Fig. 4f) depicts a consistent

distribution of copper atoms across the sample. A uniform presence of copper is indicated by consistent dot intensity, which supports the overall homogeneity of the elemental composition of the CuO NPs. The desirable characteristics of the CuO NPs greatly depend on this even distribution of copper and oxygen. The accuracy and predictable performance of the material in various applications, such as photocatalysis and sensing, is certain through sustaining a well-defined and consistent elemental composition. Any alterations to this consistency may result in differences in the functionality or activity of the nanoparticles. Therefore, one of the main factors influencing the CuO NPs' reliability and effectiveness in their intended applications is the uniformity that has been seen in the dot maps.

HRTEM studies: As seen in Fig. 5a, HRTEM specifically focused on a single particle chosen from one of these clusters. The CuO NPs have a spherical overall shape with noticeable size differences. These nanoparticles have dimensions primarily in the range between 5 and 20 nm. A clear crystalline structure can be seen in the HRTEM image, which reveals the lattice fringes inside the nanoparticles. The crystal structure is calculated from the interfringe spacing; for CuO, this typically has a monoclinic shape. When examined more closely, the surface of nanoparticles was shown to be smooth and free of large faults or defects. This indepth examination supports the finding of an aggregated configuration in which the nanoparticles are enclosed in a prominent spherical rod of around 200 nm in diameter.

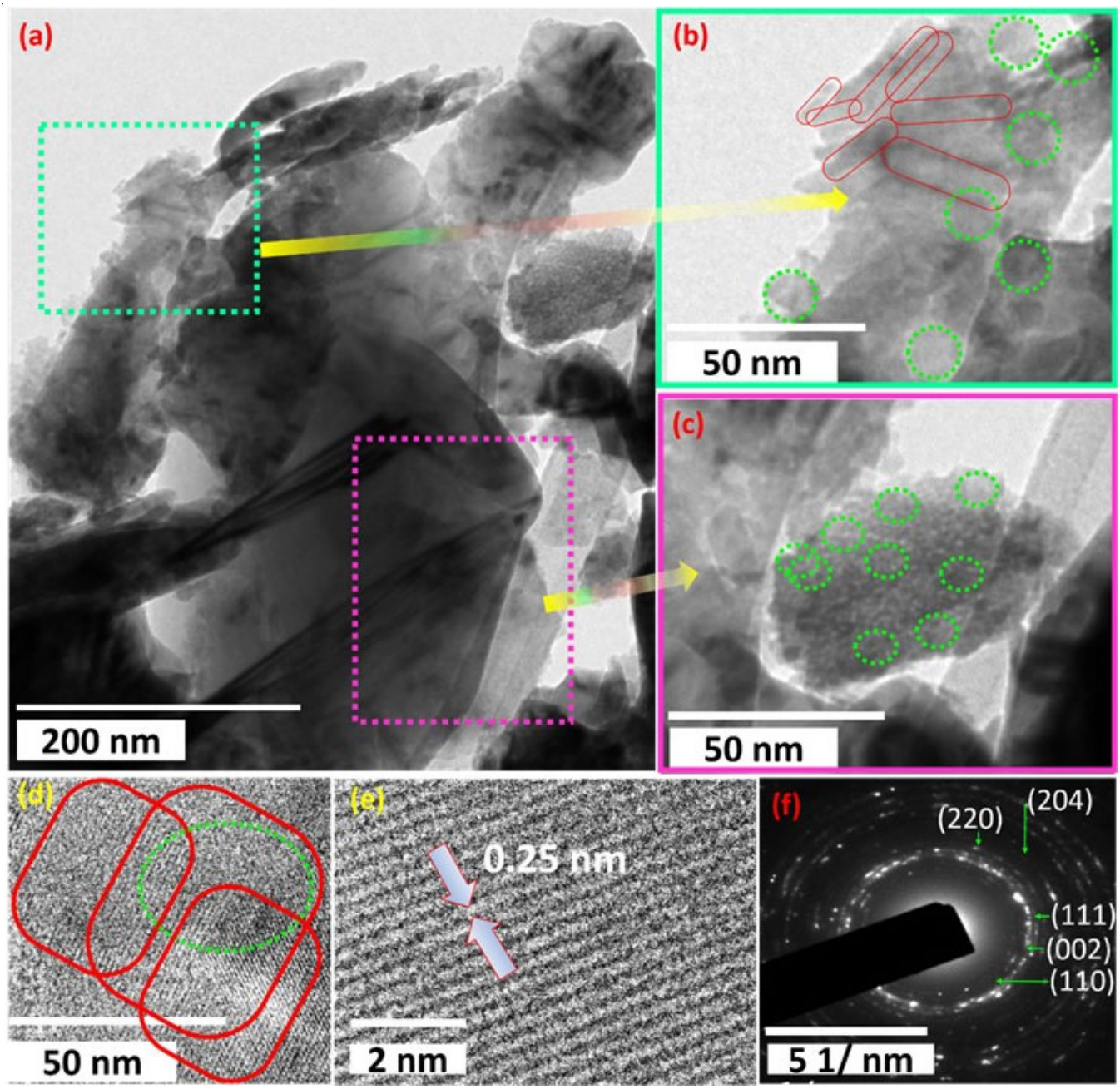

Fig. 5. The morphology of CuO NPs synthesized by *S. aromaticum* (a-c) HRTEM images; (d) particle size distribution; (e) d-spacing HRTEM and (f) SAED pattern

Interestingly, the outer edge of rod is covered with many fringes, suggesting that it may have secondary growth surrounding a core.

At higher magnification of 50 nm, Fig. 5b displays the HRTEM image of CuO NPs, which shows that a particle are quite porous having a network of interconnected pores with different shape and size. While some pores have a spherical shape and are considerably smaller, some are rather massive, resembling capsules. The pores' walls seem to have a lot of roughness and to be uneven and rough, which might be due to the presence of grains or other foreign particles. With some size fluctuation, the CuO NPs in Fig. 5c seem to be primarily spherical or somewhat elongated and range in diameter from around 2 to 10 nm. The HRTEM image in Fig. 5c also displays the lattice fringes within the nanoparticles suggesting a crystalline structure, as similar to Fig. 5a. The crystal structure may be determined from the spacing between the fringes and for CuO, it is probably monoclinic. Due to the increased magnification of 50 nm, the surface of the nanoparticles in Fig. 5c seems to be largely smooth, with scattered steps or edges evident. However, Fig. 5a provides a more comprehensive understanding of the size range and dispersion of nanoparticles within the sample.

Examining Fig. 5d, it is observed that the nanoparticles appear as dark, elongated and generally spherical, with a size distribution between 10 and 20 nm. The stability and ability to avoid aggregating are enhanced by this coating nanoparticles. Lattice fringes or the atom-by-atom lines that comprise the crystal structure of nanoparticles, are also visible in the inset of the HRTEM image. The crystal structure can be determined from the fringes' spacing. The HRTEM micrograph taken at a high magnification with a bar scale of 2 nm provides a detailed perspective of the crystallographic details of the synthesized CuO NPs as shown in Fig. 5e. Crystallite fringes are visible upon closer inspection and are highlighted by white arrows. The interplanar spacing between these fringes is consistently measured and it matches the *d*-spacing of atomic planes (0.25 nm) of the CuO monoclinic phase quite well. This alignment provides strong evidence supporting the X-ray diffraction (XRD) results and supports the unambiguous identification of the monoclinic phase. Upon close examination of the lattice fringes in the micrograph, it becomes evident that there are few defects or irregularities. However, the absence of heterojunctions or surface defects with the *S. aromaticum* extract suggests that these factors do not impact the catalytic or photocatalytic activity of the nanoparticles. As we move to Fig. 5f, HRTEM is directed towards the selected area electron diffraction (SAED) pattern, which is an essential instrument for determining a material's crystallinity. The concentric circles comprising the pattern correspond to the recognized characteristic of a polycrystalline material. Interestingly, the concentric rings in the diffraction pattern indicate that the CuO NPs are spherical. An extensive procedure was also used on the SAED patterns to gain further insight into the details of the crystallographic planes that correlate to the observed rings. This process produced more evidence supporting the monoclinic phase identification, which showed excellent agreement with the results of the XRD analysis.

Photocatalytic activity: Fig. 6a demonstrates the inherent photostability of Congo red dye, revealing a negligible concentration decrease even after 60 min of UV exposure. In contrast, Fig. 6b illustrates the remarkable photocatalytic efficacy of *S. aromaticum* extract mediated CuO NPs. Both concentrations led to substantial Congo red dye degradation, evident in the progressive reduction of 401 nm absorption peak. Remarkably, 200 mg L^{-1} dosage achieved near-complete degradation (97%) within 100 min, compared to ~76% achieved with 100 mg L^{-1} in 220 min (Fig. 6c). This superior performance at higher nanoparticle dosage stems from several factors, *e.g.* (i) increased active surface sites: a higher concentration of nanoparticles provides more surface area for dye adsorption and interaction with light-induced charge carriers, which translates to more active catalytic sites readily available for promoting the degradation process; (ii) enhanced charge separation: abundant nanoparticles lead to the increased light absorption, promoting the excitation of electrons in the CuO NPs. This creates more electron-hole pairs, which can further react with water molecules to generate highly reactive hydroxyl radicals ($OH^{\bullet}$) crucial for breaking down the dye molecules; and (iii) efficient dye adsorption: increased nanoparticle concentration facilitates greater adsorption of dye molecules onto their surfaces. This brings the dye molecules closer to the active sites on the nanoparticles, enhancing the efficiency of charge transfer and subsequent degradation. Fig. 6d further emphasizes the significant impact of nanoparticle dosage on Congo red dye removal percentage, with 200 mg L^{-1} achieving faster and more complete degradation compared to 100 mg L^{-1}. This finding aligns with prior research highlighting the crucial role of photocatalyst dosage in optimizing photocatalytic activity [26].

Comparative studies: Table-2 displays the most recent performance characteristics obtained utilizing CuO NPs as photocatalysts, together with other findings from our ongoing research for the sake of comparison. Furthermore, the present investigation demonstrates that *S. aromaticum*-mediated CuO NPs, particularly in the context of Congo red dye degradation, shows superior efficacy in comparison to alternative catalysts. Moreover, the use of CuO NPs in this study ensures rapid and efficient degradation of the dye under UV-light, with a remarkable degradation percentage of 97%.

Kinetic studies: The degradation kinetics of Congo red dye using *S. aromaticum*-mediated CuO NPs were scrutinized employing diverse kinetic models, encompassing pseudo-zero, first and second-order formulations (eqns. 4-6). These models not only factor in the variables influencing the reaction rate but also assess the actual rate at which Congo red dye interacts with *S. aromaticum*-mediated CuO NPs.

$$C_t = -k_0 t + C_0 \quad (5)$$

$$L_n C_t = -k_1 t + L_n C_0 \quad (6)$$

$$1/C_t = k_2 t + 1/C_0 \quad (7)$$

where C_0 and C_t denote concentrations at t = 0 and various time points during the reaction, respectively. The response rate coefficients are represented by k_0, k_1 and k_2. Fig. 7 illustrates the kinetic modelling for Congo red dye degradation facilitated

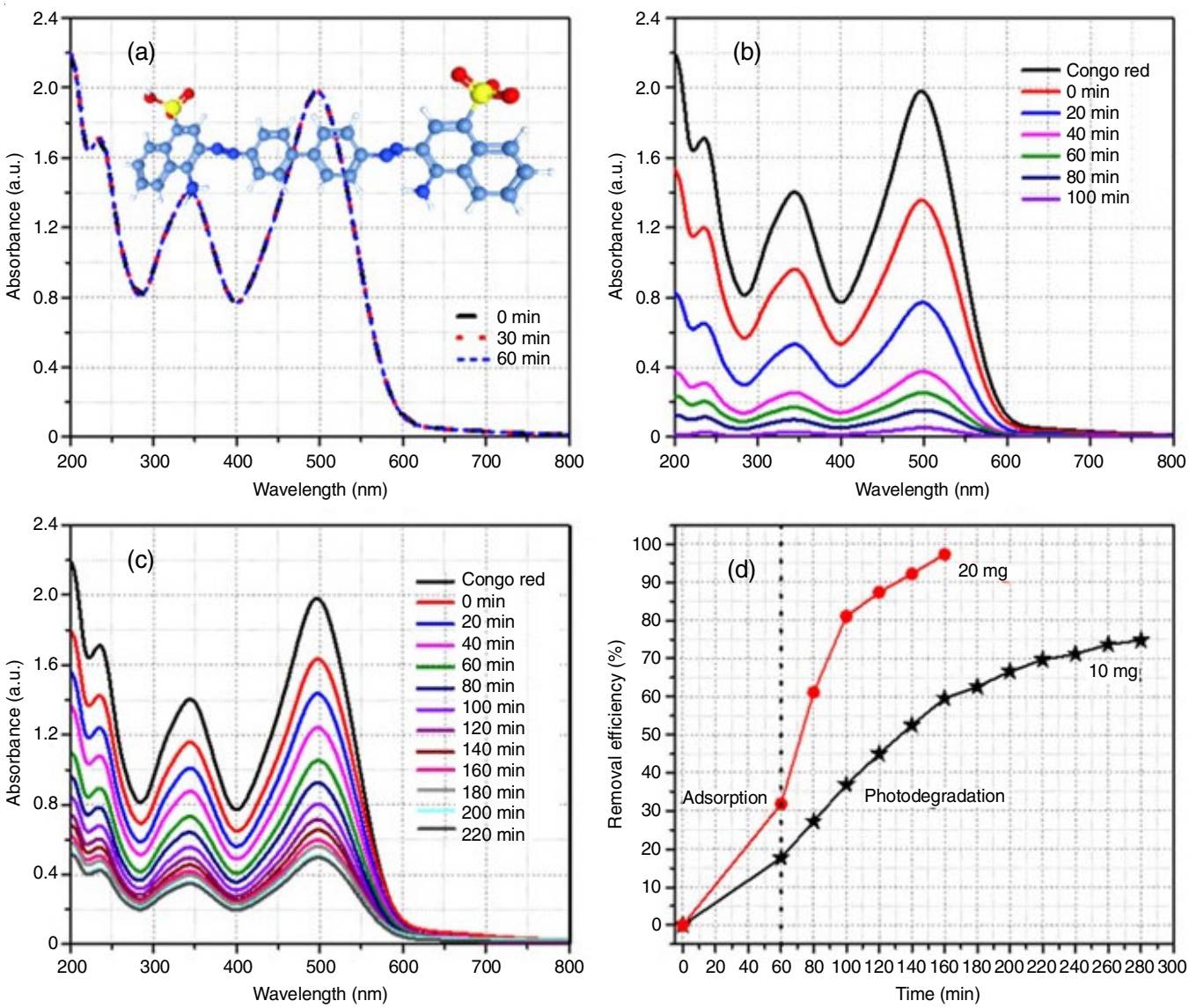

Fig. 6. Photocatalytic degradation of Congo red dye *via S. aromaticum* mediated CuO NPs (a) Congo red dye under UV light, (b-c) different dosage of photocatalyst and (d) dye removal percentage-wise

TABLE-2
COMPARATIVE ANALYSIS OF PHOTOCATALYTIC DEGRADATION ACROSS VARIOUS POLLUTANTS EMPLOYING VARIOUS CATALYSTS

Catalyst used	Pollutant used	Degradation (%)	Time (min)	Source of light	Ref.
CuO NPs	Acid red 88 dye	96.35	120	UV-light	[27]
Ag-TiO_2 NPs	Acid red 88 dye	65.00	70	UV-light	[28]
CuO NPs	Methyl orange	96.00	120	UV-light	[29]
CuO NPs	Methyl orange	45.23	60	UV-light	[30]
CuO NPs	Methyl orange	31.95	60	Sunlight	[30]
CuO NPs	Nile blue	93.00	120	Solar light	[31]
CuO NPs	Reactive yellow-160	81.00	120	Solar light	[31]
Cu_2O-Cu NCs	Methyl blue	50.00	90	Visible light	[32]
TiO_2	Malachite green	75.00	95	UV-light	[33]
CuO nano leaves	Methyl blue	89.00	180	UV-light	[34]
CuO nano leaves	Methylene violet	96.00	180	UV-light	[34]
Zn-Mn	Malachite green	93.00	120	UV-light	[35]
CuO NPs	Methyl blue	93.00	120	Sunlight	[36]
CuO NPs	Methyl red	90.00	120	Sunlight	[36]
CuO NPs	Congo red	85.00	120	Sunlight	[36]
CuO NPs	Congo red	97.00	100	UV-light	This study

by *S. aromaticum*-mediated CuO NPs, where the slope of the graphs corresponds to the reaction rate. Table-3 presents the kinetic rate response values obtained using pseudo-zero, first and second-order models. The pseudo-first-order model exhibited reasonable agreement with the experimental data in comparison to other kinetic models. The influence of *S. aromaticum* mediated CuO NPs dosages (100 and 200 mg L^{-1}) on the photodegradation rate of Congo red dye was examined. The graphs indicated that higher concentrations of green synthesized CuO NPs (200 mg L^{-1}) enhanced the reaction rate constant values. At a concentration of 200 mg L^{-1}, the reaction rate was highest ($k_1 = 0.03077$ min^{-1}), leading to the fastest photocatalytic degradation of the dye. The rapid removal of 97% of Congo red dye in 100 min highlighting the efficacy of *S. aromaticum*-mediated CuO NPs as photocatalysts. The dosage of the specific contaminant in the effluent significantly influences photodegradation efficiency [37]. Using pseudo-first-order or Langmuir kinetic models may shed light on rapid response rates at large contaminant dosages, which cannot be accurately explained by pseudo zero-order modeling [38]. The reaction rate tends to increase with an increase in the catalyst dose until deviation occurs, representing light scattering or reduced transparency. The rise in the catalyst amount hinders light penetration further into the process medium [39].

To evaluate sustainability and practicality, seven consecutive rounds of the photodegradation process at a concentration of 200 mg L^{-1} were employed. Fig. 7d demonstrates that even after seven cycles, the removal efficiency of Congo red dye remained

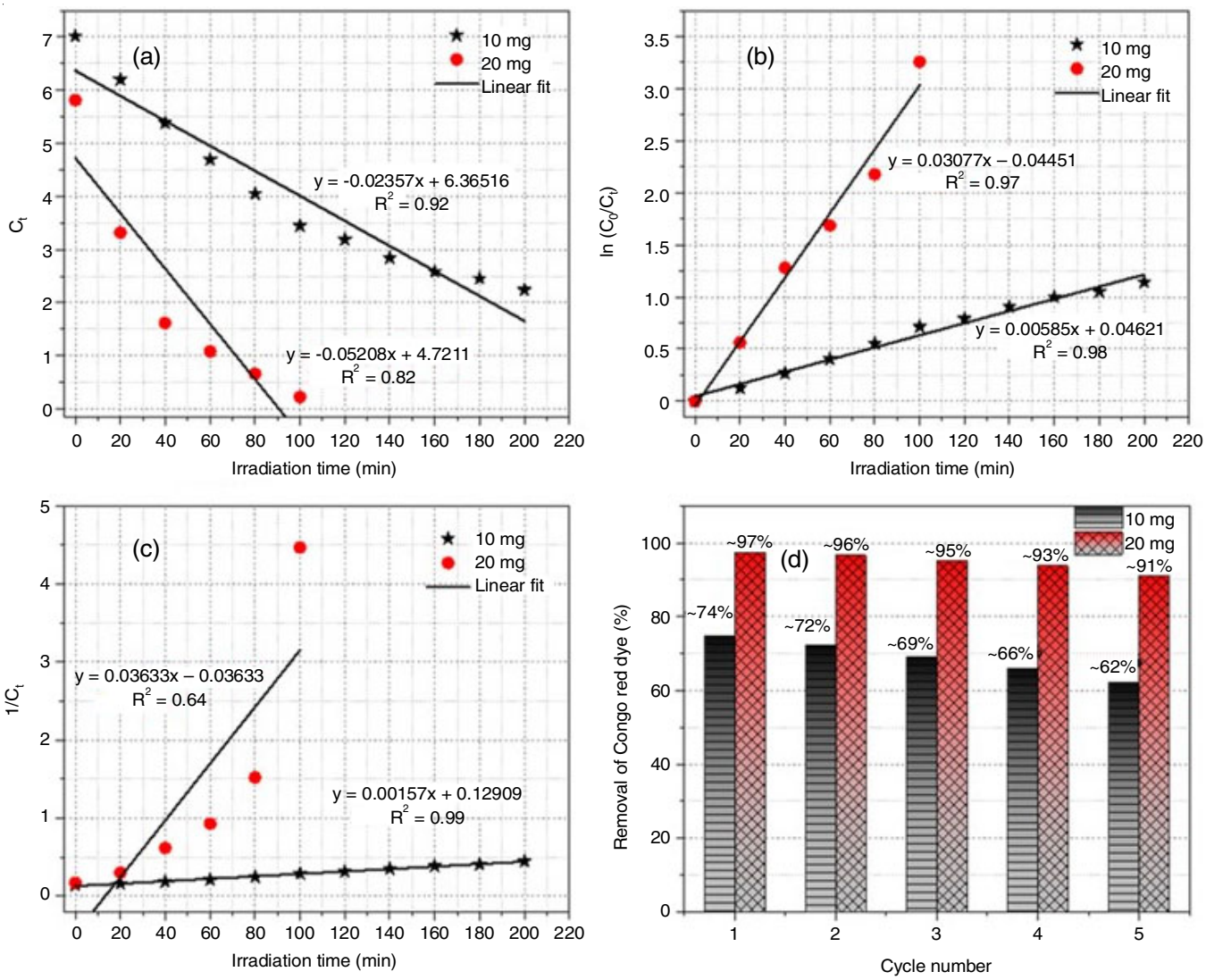

Fig. 7. Kinetic modeling of reactive yellow dye photodegradation: (a) pseudo-zero-order, (b) first order, (c) second order and (d) recyclability

TABLE-3
DEGRADATION KINETIC MODEL PARAMETERS DATA OF *S. aromaticum* MEDIATED CuO NPs

Catalyst dose (mg/L)	Pseudo-zero-order		Pseudo-first-order		Pseudo-second-order	
	k_0 (mg/L·min)	R^2	k_1 (min^{-1})	R^2	k_2 (L/mg·min)	R^2
100	0.02357	0.92	0.00585	0.98	0.00157	0.64
200	0.05208	0.82	0.03077	0.97	0.03633	0.99

above 91%. The slight decrease in the photocatalyst's removal effectiveness suggests that prolonged usage may have led to the blocking of some active surface areas on the CuO surface.

Mechanism: Fig. 8 delineates the efficient photocatalytic degradation mechanism of Congo red dye *via S. aromaticum*-mediated CuO NPs. Under exposure to UV radiation, the surface of the nanoparticles generate electron-hole pairs. The generated electrons are subsequently transferred to the conduction band of CuO. The reaction of these electrons with oxygen leads to the generation of superoxide ions. The positive charge on the CuO surface attracts electrons from the surroundings or air, resulting in the formation of hydroxyl radicals. These hydroxyl radicals and superoxide ions effectively react with Congo red dye molecules, breaking them down into less harmful compounds. In addition to providing a high specific surface area for the CuO NPs, the phytochemicals in *S. aromaticum* extract enhance the photocatalytic process by donating electrons and accepting holes from the oxygen and carbon atoms.

The photocatalytic mechanism of *S. aromaticum*-mediated CuO NPs are elucidated through the following steps:

a) Electrons and holes are generated when UV light interacts with the surface of nanoparticles.

$$h\nu_{UV} + SA/CuO \longrightarrow e^- + h^+$$

b) Hydroxyl radicals are produced when oxygen reacts with humid air.

$$h^+ + H_2O \longrightarrow H^+ + OH^\bullet$$

c) Superoxide is produced during the reduction reaction.

$$e^- + O_2 \longrightarrow O_2^{\bullet-}$$

d) Recombination of electrons and holes may occur, triggering subsequent reactions.

$$O_2^{\bullet-} + H^+ \longrightarrow HO_2^\bullet$$

$$O_2^{\bullet-} + H^+ + HO_2^\bullet \longrightarrow H_2O_2 + O_2$$

$$H_2O_2 + h\nu \longrightarrow 2OH^\bullet$$

$$e^- + HO_2^\bullet \longrightarrow HO^- + H^+$$

$$h^+ + OH^- \longrightarrow OH$$

e) Dye elimination through oxidizing agents, where reactive species (O_2 or $OH^\bullet$) combine with Congo red dye compounds, producing simpler compounds than just H_2O and CO_2.

Conclusion

This work revealed the interesting prospects for CuO NPs produced by *Syzygium aromaticum* bud extract. The indepth study found some unique features, including a small crystallite size of 7.89 nm and the presence of monoclinic phase, which is different from the bulk CuO NPs. A thorough FTIR study supported the successful incorporation of phytochemicals into the CuO surface. Additionally, the spherical nanostructure was visualized and explained using FESEM and HR-TEM micro-

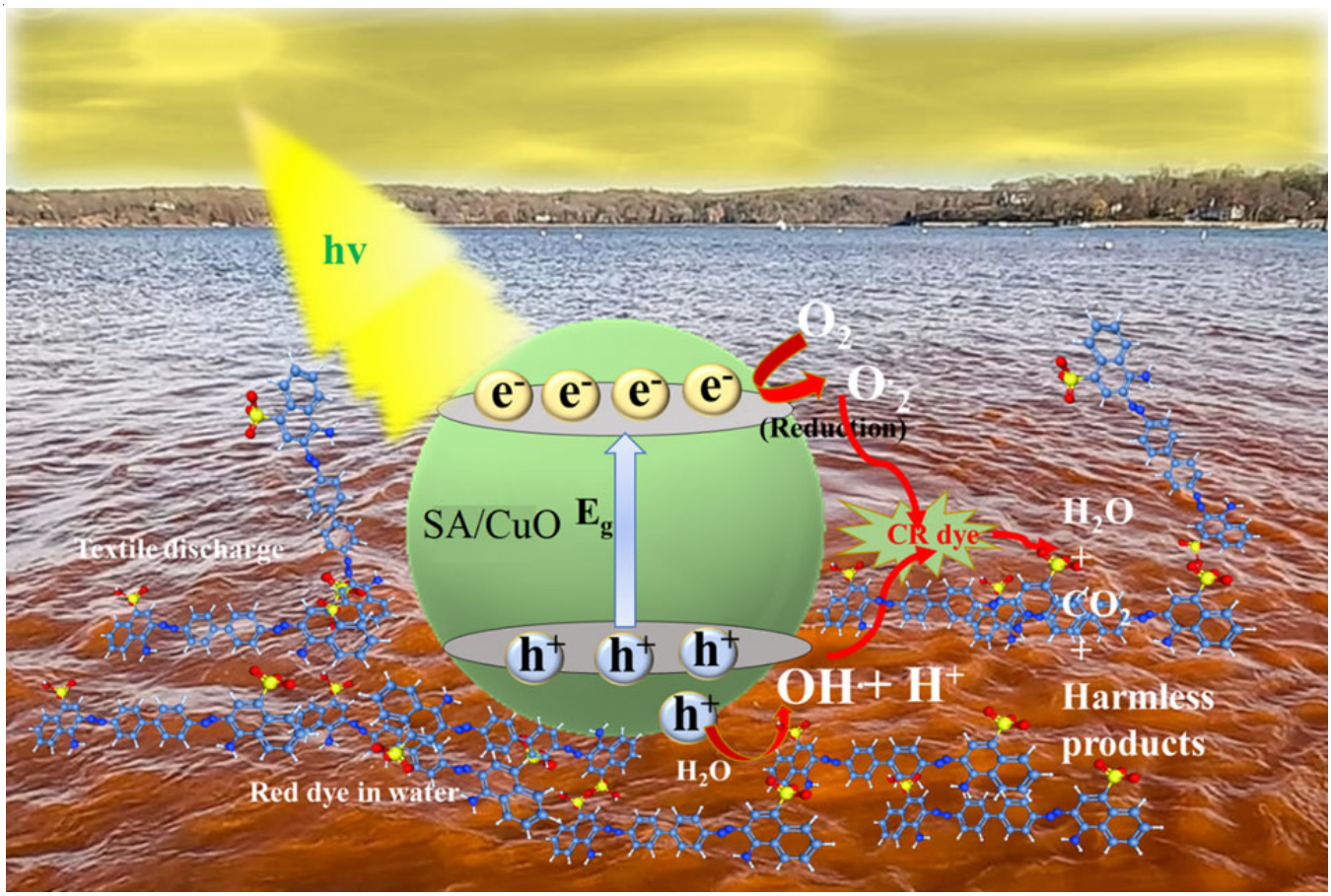

Fig. 8. Mechanism of photocatalytic degradation

graphs. This study demonstrates the exceptional efficacy of employing photocatalytic activity to break down the highly resistant Congo red dye molecules under UV radiation. The enhanced performance of these nanoparticles is due to their unique features, including their small crystallite size, high crystallinity, correct band-gap energy, custom surfaces and complex nanostructure. The study sheds light on *S. aromaticum* mediated CuO NPs as a potential solution to environmental issues and also gives details regarding the green synthesis process. These discoveries provide crucial knowledge and enable the development of sustainable and highly effective photocatalysts.

CONFLICT OF INTEREST

The authors declare that there is no conflict of interests regarding the publication of this article.

REFERENCES

1. N.B. Jadeja, T. Banerji, A. Kapley and R. Kumar, *Water Secur.*, **16**, 100119 (2022); https://doi.org/10.1016/j.wasec.2022.100119
2. R. Jamee and R. Siddique, *Eur. J. Microbiol. Immunol.*, **9**, 114 (2019); https://doi.org/10.1556/1886.2019.00018
3. S. Benkhaya, S. M'Rabet and A. El Harfi, *Heliyon*, **6**, e03271 (2020); https://doi.org/10.1016/j.heliyon.2020.e03271
4. G. Dong, B. Chen, B. Liu, L.J. Hounjet, Y. Cao, S.R. Stoyanov, M. Yang and B. Zhang, *Water Res.*, **211**, 118047 (2022); https://doi.org/10.1016/j.watres.2022.118047
5. J. Borah and B.K. Sarma, *Mater. Today Proc.*, **65**, 2523 (2022); https://doi.org/10.1016/j.matpr.2022.04.509
6. A.E. Guardia, M.V. Beligni, N. Cortéz and J.P. Busalmen, *Electrochim. Acta*, **355**, 136757 (2020); https://doi.org/10.1016/j.electacta.2020.136757
7. M. Nesa, M.A. Momin, M. Sharmin and A.H. Bhuiyan, *Chem. Phys.*, **528**, 110536 (2020); https://doi.org/10.1016/j.chemphys.2019.110536
8. Q. Zhang, L. Xu, P. Ning, J. Gu and Q. Guan, *Appl. Surf. Sci.*, **317**, 955 (2014); https://doi.org/10.1016/j.apsusc.2014.09.017
9. R. Djebian, B. Boudjema, A. Kabir and C. Sedrati, *Solid State Sci.*, **101**, 106147 (2020); https://doi.org/10.1016/j.solidstatesciences.2020.106147
10. J. Xie, C. Zhang and T.D. Waite, *Water Res.*, **217**, 118425 (2022); https://doi.org/10.1016/j.watres.2022.118425
11. A.K. Ambedkar, D. Gautam, S. Vikal, M. Singh, A. Kumar, A. Sanger, K. Sharma, B.P. Singh and Y.K. Gautam, *ACS Omega*, **8**, 29663 (2023); https://doi.org/10.1021/acsomega.3c03765
12. H.T. Liu, S.M. Zheng, H.F. Xiong, M.S. Alwahibi and X.L. Niu, *Arab. J. Chem.*, **13**, 6995 (2020); https://doi.org/10.1016/j.arabjc.2020.07.006
13. D.M. Nzilu, E.S. Madivoli, D.S. Makhanu, S.I. Wanakai, G.K. Kiprono and P.G. Kareru, *Sci. Rep.*, **13**, 14030 (2023); https://doi.org/10.1038/s41598-023-41119-z
14. H. Veisi, B. Karmakar, T. Tamoradi, S. Hemmati, M. Hekmati and M. Hamelian, *Sci. Rep.*, **11**, 1983 (2021); https://doi.org/10.1038/s41598-021-81320-6
15. K. Gebremedhn, M.H. Kahsay and M. Aklilu, *J. Pharm. Pharmacol.*, **7**, 327 (2019); https://doi.org/10.17265/2328-2150/2019.06.007
16. S. Honary, C.H. Barabadi, E. Gharaei and F. Naghibi, *Dig. J. Nanomater. Biostruct.*, **7**, 999 (2012).
17. W.W. Andualem, F.K. Sabir, E.T. Mohammed, H.H. Belay and B.A. Gonfa, *J. Nanotechnol.*, **2020**, 2932434 (2020); https://doi.org/10.1155/2020/2932434
18. T.B. Vidovix, H.B. Quesada, E.F.D. Januário, R. Bergamasco and A.M.S. Vieira, *Mater. Lett.*, **257**, 126685 (2019); https://doi.org/10.1016/j.matlet.2019.126685
19. R. Usha, E. Prabu, M. Palaniswamy, C.K. Venil and R. Rajendran, *Global J. Biotechnol. Biochem.*, **5**, 153 (2010).
20. K. Ganesan, V.K. Jothi, A. Natarajan, A. Rajaram, S. Ravichandran and S. Ramalingam, *Arab. J. Chem.*, **13**, 6802 (2020); https://doi.org/10.1016/j.arabjc.2020.06.033
21. H. Kaur, J. Singh, P. Rani, N. Kaur, S. Kumar and M. Rawat, *J. Mol. Liq.*, **355**, 118966 (2022); https://doi.org/10.1016/j.molliq.2022.118966
22. V.K. Pandey, S. Srivastava, Ashish, K.K. Dash, R. Singh, A.H. Dar, T. Singh, A. Farooqui, A.M. Shaikh and B. Kovacs, *Heliyon*, **10**, e22437 (2024); https://doi.org/10.1016/j.heliyon.2023.e22437
23. S. Sathiyavimal, S. Vasantharaj, V. Veeramani, M. Saravanan, G. Rajalakshmi, T. Kaliannan, F.A. Al-Misned and A. Pugazhendhi, *J. Environ. Chem. Eng.*, **9**, 105033 (2021); https://doi.org/10.1016/j.jece.2021.105033
24. B. Amelia, E. Saepudin, A.H. Cahyana, D.U. Rahayu and A.S. Sulistyoningrum, *AIP Conf. Proc.*, **1862**, 030082 (2017); https://doi.org/10.1063/1.4991186
25. H. Sajjad, A. Sajjad, R.T. Haya, M.M. Khan and M. Zia, *Comp. Biochem. Physiol. C Toxicol. Pharmacol.*, **271**, 109682 (2023); https://doi.org/10.1016/j.cbpc.2023.109682
26. I. Ahmad, Y. Zou, J. Yan, Y. Liu, S. Shukrullah, M.Y. Naz, H. Hussain, W.Q. Khan and N.R. Khalid, *Adv. Colloid Interface Sci.*, **311**, 102830 (2023); https://doi.org/10.1016/j.cis.2022.102830
27. H.N. Jayasimha, K.G. Chandrappa, P.F. Sanaulla and V.G. Dileepkumar, *Sens. Int.*, **5**, 100254 (2024); https://doi.org/10.1016/j.sintl.2023.100254
28. S. Anandan, P. Sathish Kumar, N. Pugazhenthiran, J. Madhavan and P. Maruthamuthu, *Sol. Energy Mater. Sol. Cells*, **92**, 929 (2008); https://doi.org/10.1016/j.solmat.2008.02.020
29. F. Keivani Nahr, B. Ghanbarzadeh, H. Samadi Kafil, H. Hamishehkar and M. Hoseini, *J. Dispers. Sci. Technol.*, **42**, 1 (2020); https://doi.org/10.1080/01932691.2019.1658597
30. A. Ikram, S. Jamil and M. Fasehullah, *Mater. Innov.*, **2**, 115 (2022); http://doi.org/10.54738/MI.2022.2401
31. J. Singh, V. Kumar, K.-H. Kim and M. Rawat, *Environ. Res.*, **177**, 108569 (2019); https://doi.org/10.1016/j.envres.2019.108569
32. S. Li, Q. Lin, X. Liu, L. Yang, J. Ding, F. Dong, Y. Li, M. Irfan and P. Zhang, *RSC Adv.*, **8**, 20277 (2018); https://doi.org/10.1039/C8RA03117G
33. M. Asiltürk, F. Sayilkan and E. Arpaç, *J. Photochem. Photobiol. Chem.*, **203**, 64 (2009); https://doi.org/10.1016/j.jphotochem.2008.12.021
34. S. Sonia, S. Poongodi, P.S. Kumar, D. Mangalaraj, N. Ponpandian and C. Viswanathan, *Mater. Sci. Semicond. Process.*, **30**, 585 (2015); https://doi.org/10.1016/j.mssp.2014.10.012
35. N. Zada, I. Khan and K. Saeed, *Sep. Sci. Technol.*, **52**, 1477 (2017); https://doi.org/10.1080/01496395.2017.1285920
36. R. Katwal, H. Kaur, G. Sharma, M. Naushad and D. Pathania, *J. Ind. Eng. Chem.*, **31**, 173 (2015); https://doi.org/10.1016/j.jiec.2015.06.021
37. M.A. Al-Nuaim, A.A. Alwasiti and Z.Y. Shnain, *Chem. Zvesti*, **77**, 677 (2023); https://doi.org/10.1007/s11696-022-02468-7
38. E.D. Revellame, D.L. Fortela, W. Sharp, R. Hernandez and M.E. Zappi, *Clean. Eng. Technol.*, **1**, 100032 (2020); https://doi.org/10.1016/j.clet.2020.100032
39. P. Murugesan, D.K. Brunda, J.A. Moses and C. Anandharamakrishnan, *Food Control*, **123**, 107748 (2021); https://doi.org/10.1016/j.foodcont.2020.107748